Electronic Supplementary Information

MoSe₂ Quantum Dots Modified Hole Extraction Layer Enables Binary Organic Solar Cells with Improved Efficiency and Stability

Hong Lian,[‡a,b] Mingao Pan,[‡c] Jinba Han,[a] Xiaozhe Cheng,[a] Jiaen Liang,[c] Wenqiang Hua,[d] Yongquan Qu,[a] Yucheng Wu,[a] Qingchen Dong,*[a,b] Bin Wei,*[b] He Yan,*[c] and Wai-Yeung Wong*[e]

[a]MOE Key Laboratory of Interface Science and Engineering in Advanced Materials, Taiyuan University of Technology, 79 Yingze West Street, Taiyuan, 030024, China. E-mail: dongqingchen@tyut.edu.cn.

[b]MOE Key Laboratory of Advanced Display and System Applications, Shanghai University, Shanghai, 200072, China. E-mail: bwei@shu.edu.cn.

[c]Department of Chemistry and Hong Kong Branch of Chinese National Engineering Research Center for Tissue Restoration & Reconstruction, Hong Kong University of Science and Technology, Clear Water Bay, Kowloon, Hong Kong. China. E-mail: hyan@ust.hk.

[d]Shanghai Advanced Research Institute, Chinese Academy of Sciences, 201210, China.

[e]Department of Applied Biology and Chemical Technology and Research Institute for Smart Energy (RISE), The Hong Kong Polytechnic University, Hung Hom, Hong Kong, China, E-mail: wai-yeung.wong@polyu.edu.hk

[‡]These people contribute equally to this work.

Chart titles

Fig. S1. EDS elemental maps measurement.

Fig. S2. XPS analysis and schematic diagrams of post heat-treated thin film of $MoSe_2$ QDs.

Fig. S3. Films characterizations of HEL.

Fig. S4. J–V curves.

Fig. S5. Distribution histograms of the PCE for 50 devices of PEDOT:PSS and $MoSe_2$ QDs/PEDOT:PSS based solar cells.

Fig. S6. G_{max} and $P(E,T)$ versus rotation speeds, J_{sc} and V_{oc} versus I.

Fig. S7. The dark J−V characteristics and the hole only devices.

Fig. S8. Electric impedance spectra, PL spectra and the TRPL decay profiles.

Fig. S9. 2D GIWAXS images and profiles.

Fig. S10. 2D GISAXS images.

Fig. S11. Photovoltaic performance based on the blend system PBDB-T/ITIC.

Fig. S12. Stability measurement.

Fig. S13. Photovoltaic performance based on the blend system P3HT/PC_{61}BM and PTB7-Th/PC_{71}BM.

List of tables

Table S1. Parameters of the testing liquids of water and EG.

Table S2. The contact angle and surface energy of different materials.

Table S3. The interface energy between two different materials.

Table S4. Summary of device performances of PM6:Y6 based OSCs

Table S5. Comparison of the device parameters.

Table S6. Hole mobility and conductivity.

Table S7. Photovoltaic parameters of the optimal OSCs based on others systems.

S1. Experimental details.

S2. The XPS characterization of post heat-treated thin film of MoSe$_2$ QDs.

S3. The calculation of G_{max} and P(E,T).

S4. The relationship of J_{sc}, V_{oc} and I.

S5. The surface energy and interfacial energy calculations.
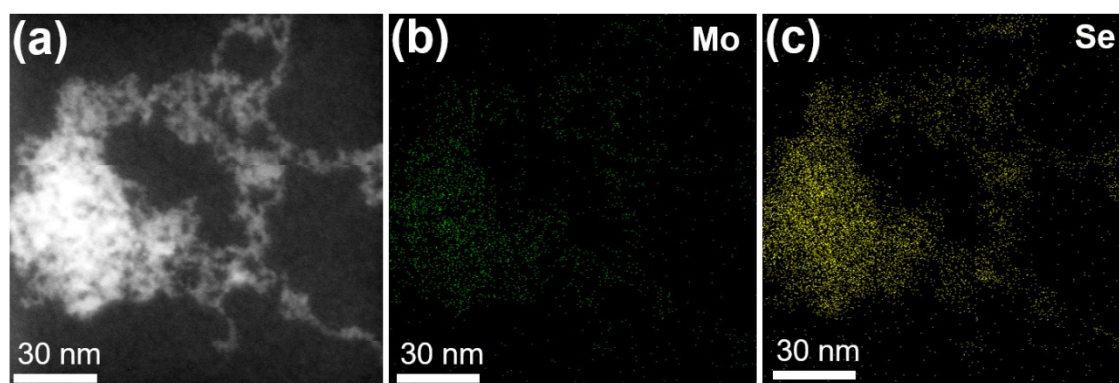
Fig. S1. The HR-TEM images measured for the MoSe$_2$ QDs. The corresponding EDS elemental maps of (a) indicating the homogeneous distribution of (b) Mo (in green) and (c) Se (in yellow).
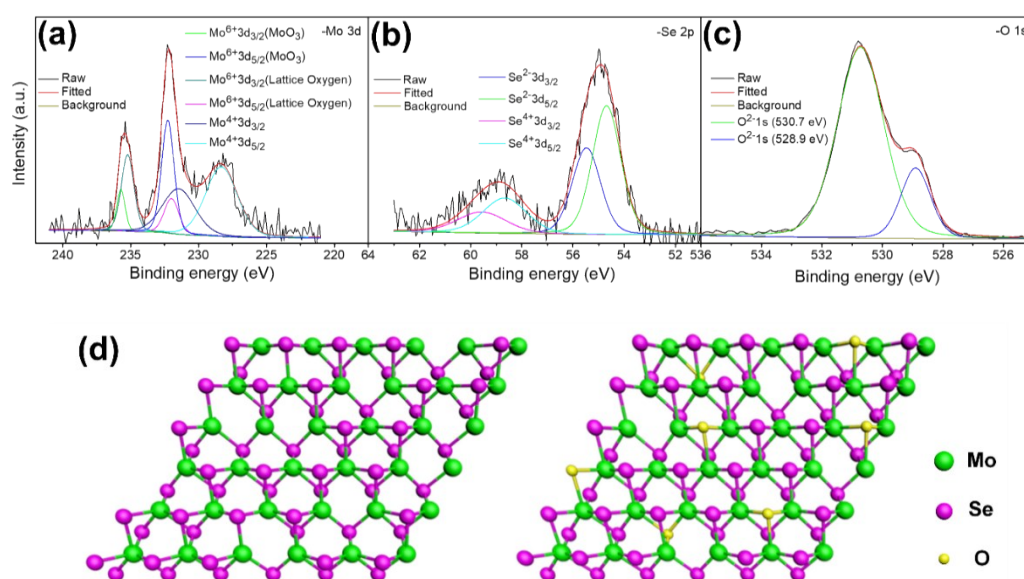
Fig. S2. (a) Mo 3d, (b) Se 2p and (c) O 1s XPS analysis of MoSe$_2$ QDs. (d) Schematic diagrams of oxygen atom passivating the structural defects: before (left) and after (right) heat treatment.
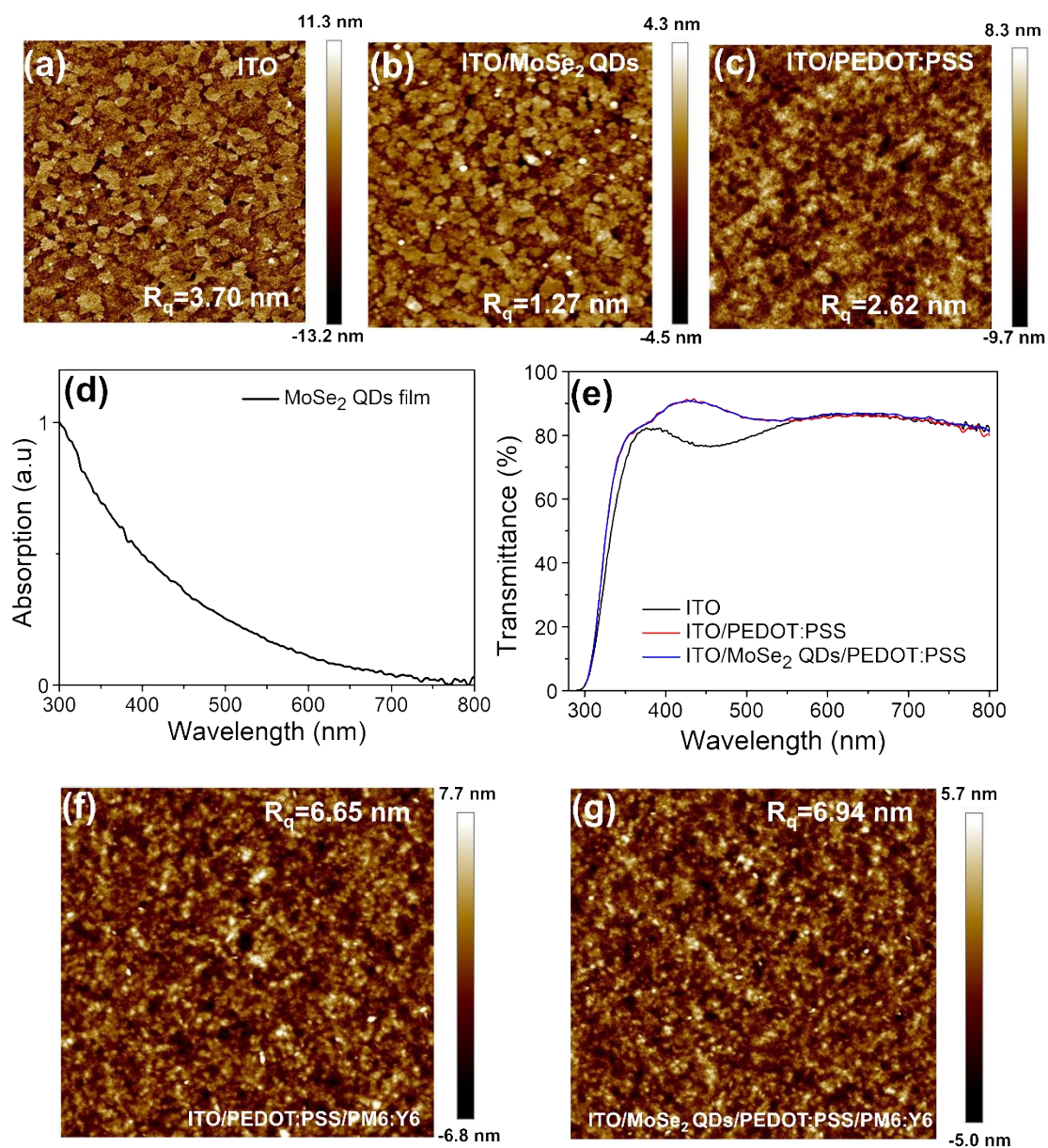
Fig. S3. (a-c) 5 um^2 tapping mode AFM images of ITO, ITO/MoSe$_2$ QDs, ITO/PEDOT:PSS film. (d) The normalized UV-vis absorption spectrum of MoSe$_2$ QDs neat film. (e) The transmission spectra of ITO, ITO/PEDOT:PSS and ITO/MoSe$_2$ QDs/PEDOT:PSS. AFM images of (f) PEDOT:PSS/BHJ and (g) MoSe$_2$ QDs/PEDOT:PSS/BHJ (bilayer) on top

ITO/glass substrate.
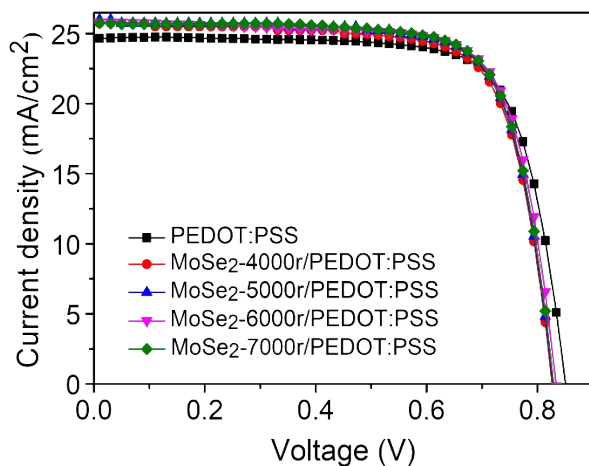
Fig. S4. *J–V* curves obtained for the PEDOT:PSS based control cell and the MoSe$_2$ QDs/PEDOT:PSS based OSCs fabricated at the rotation speeds of 4000, 5000, 6000, and 7000 rpm, respectively.
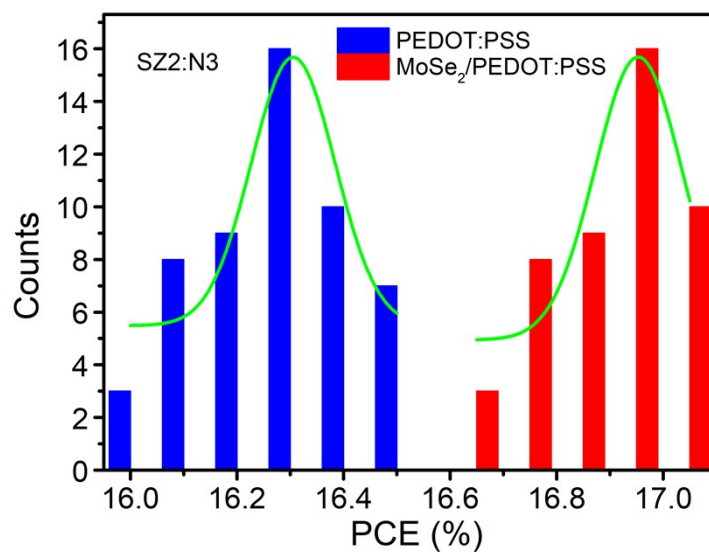
Fig. S5. Distribution histograms of the PCE for 50 devices of PEDOT:PSS and MoSe$_2$ QDs/PEDOT:PSS based solar cells.
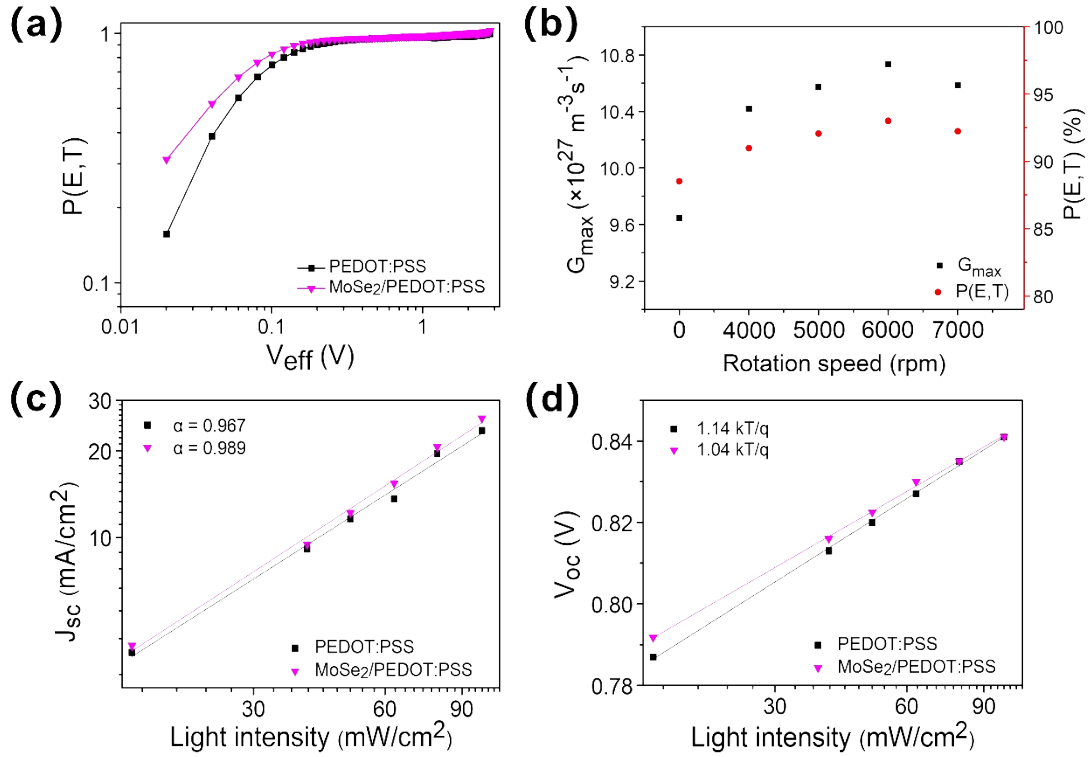
Fig. S6. (a) The *P(E,T)* versus *V_{eff}*. (b) The values of *G_{max}* and *P(E,T)* obtained for the PEDOT:PSS based control cell (here displayed as the points of rotation speed = 0) and the MoSe$_2$ QDs/PEDOT:PSS based OSCs fabricated at rotation speeds of 4000, 5000, 6000, and 7000 rpm, respectively. (c) *J_{sc}* and (d) *V_{oc}* on light intensity for devices with or without MoSe$_2$ QDs.
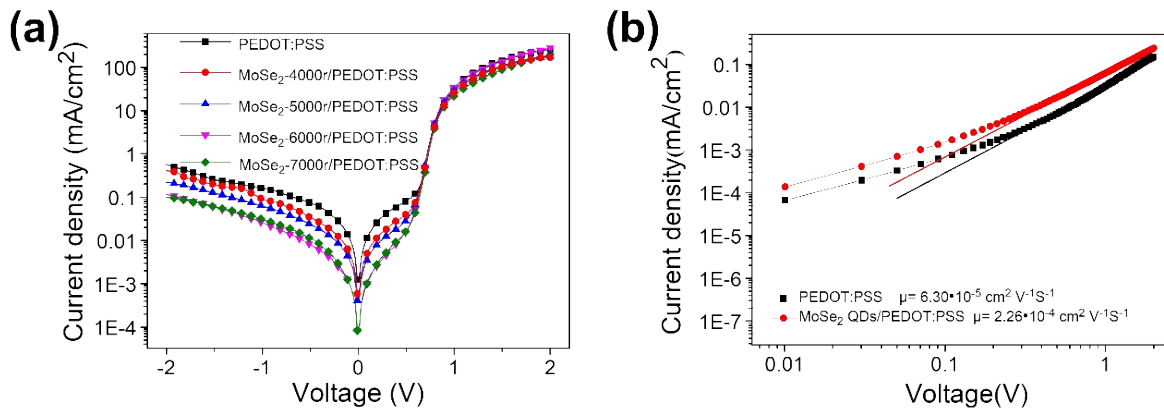
Fig. S7. The dark *J−V* characteristics of all cells. (b) *J-V* characteristics of the hole only

devices with or without MoSe$_2$ QDs.
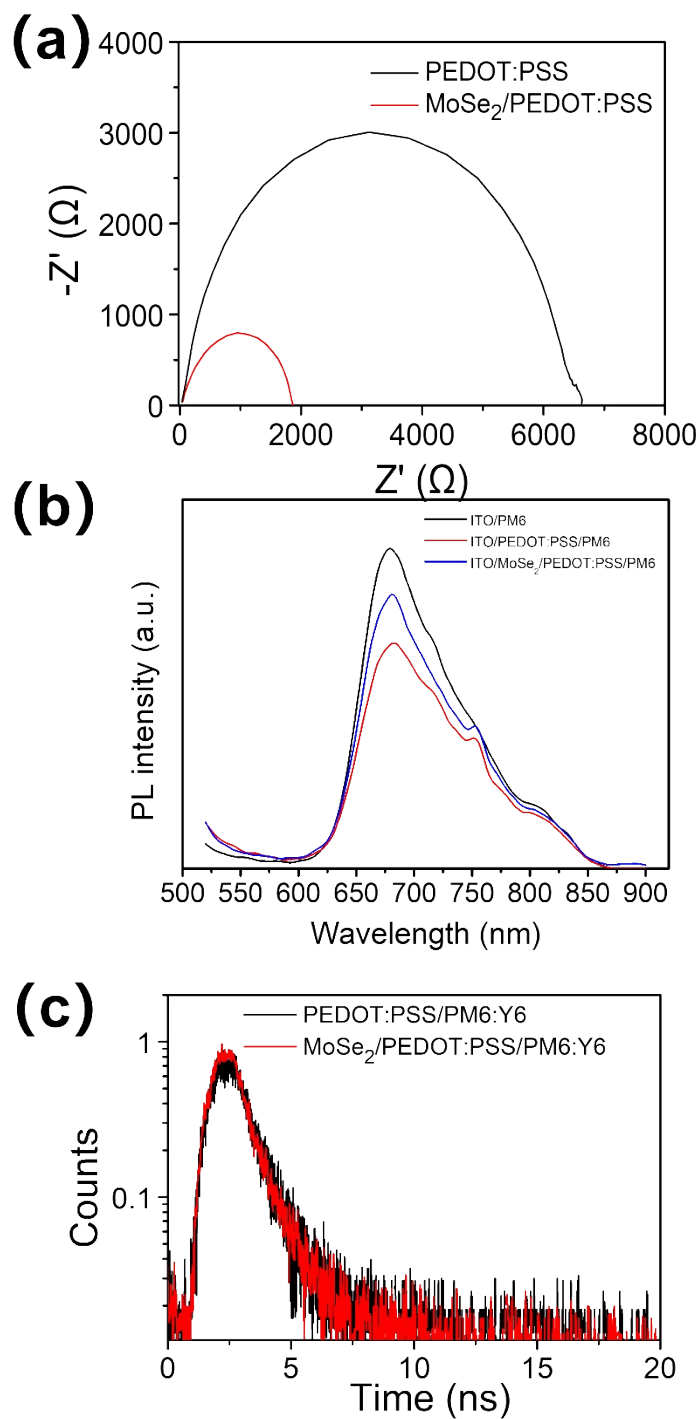
Fig. S8. (a) Electric impedance spectra for the MoSe$_2$ QDs/PEDOT:PSS HEL based cells and the control cell. (b) PL spectra of ITO/PM6, ITO/PEDOT:PSS/PM6 and ITO/MoSe$_2$ QDs/PEDOT:PSS/PM6 thin films. (c) The TRPL decay profiles of PEDOT:PSS/PM6:Y6 and

MoSe$_2$ QDs/PEDOT:PSS/PM6:Y6 thin films deposited on quartz glasses.
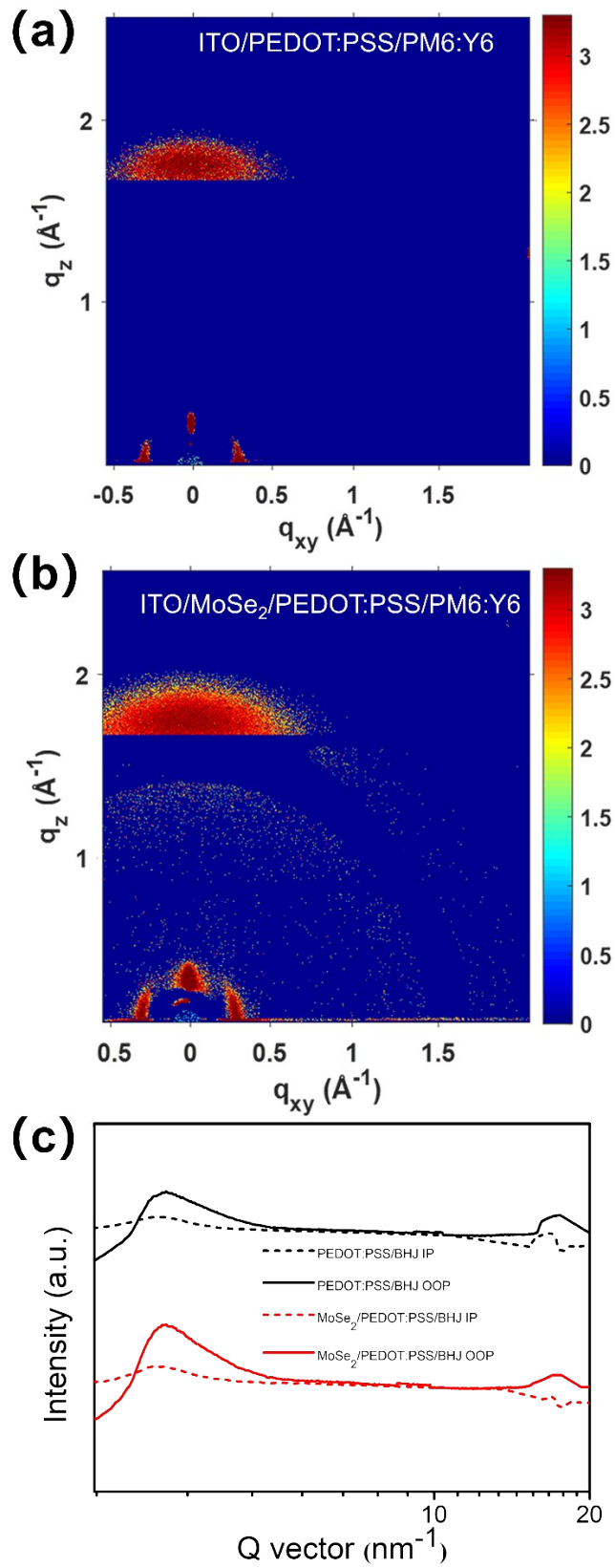
Fig. S9. GIWAXS images of (a) ITO/PEDOT:PSS/PM6:Y6, and (b) ITO/MoSe$_2$

QDs/PEDOT:PSS/PM6:Y6 thin films. (c) GIWAXS intensity profiles along the in-plane (dotted line) and out-of-plane (solid line) directions.
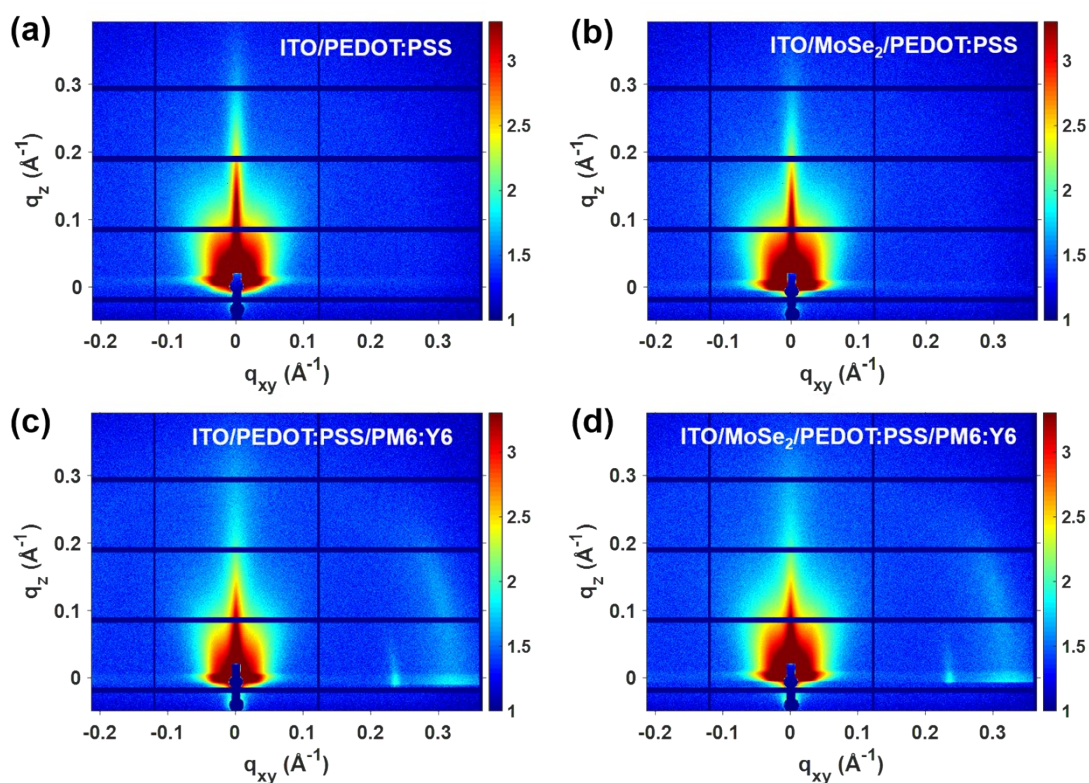
Fig. S10. 2D GISAXS images of (a) ITO/PEDOT:PSS, (b) ITO/MoSe$_2$ QDs/PEDOT:PSS, (c) ITO/PEDOT:PSS/PM6:Y6, and (d) ITO/MoSe$_2$ QDs/PEDOT:PSS/PM6:Y6 thin films.
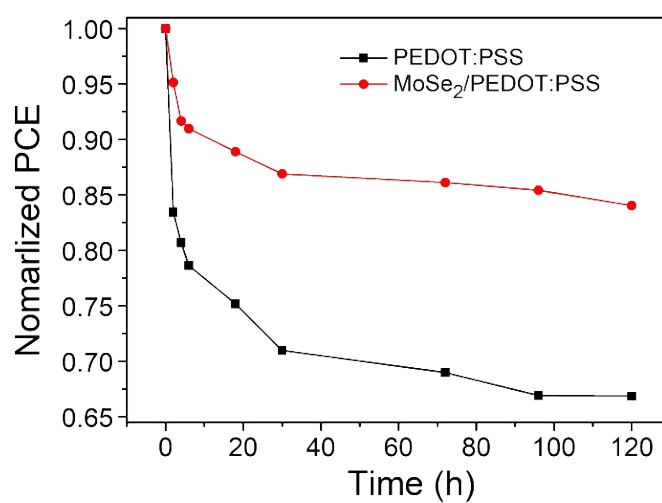
Fig. S11. Normalized stability curves of PCE measured for control cell and the champion cell

based on MoSe$_2$ QDs/PEDOT:PSS.
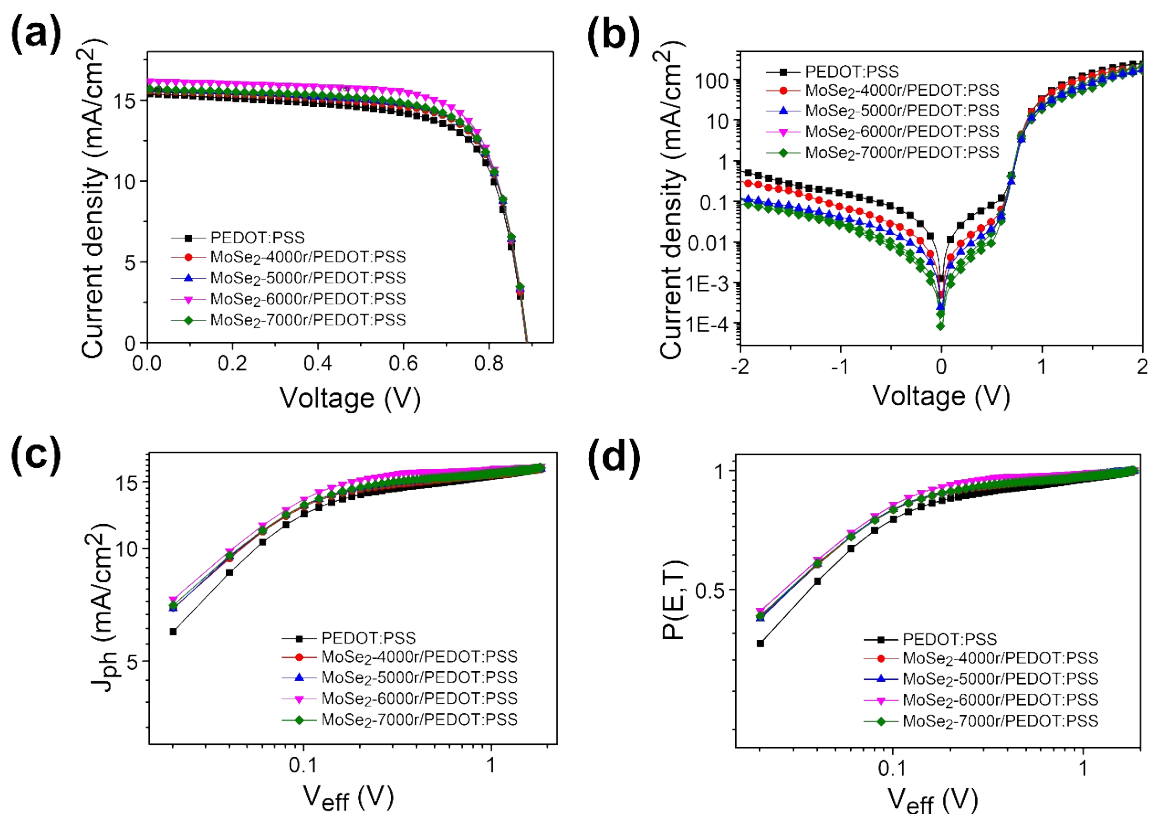
Fig. S12. (a) *J–V* curves and (b) dark curves based on the blend system PBDB-T/ITIC with or without MoSe$_2$ QDs. (c) J_{ph} and (d) *P (E,T)* versus V_{eff}.
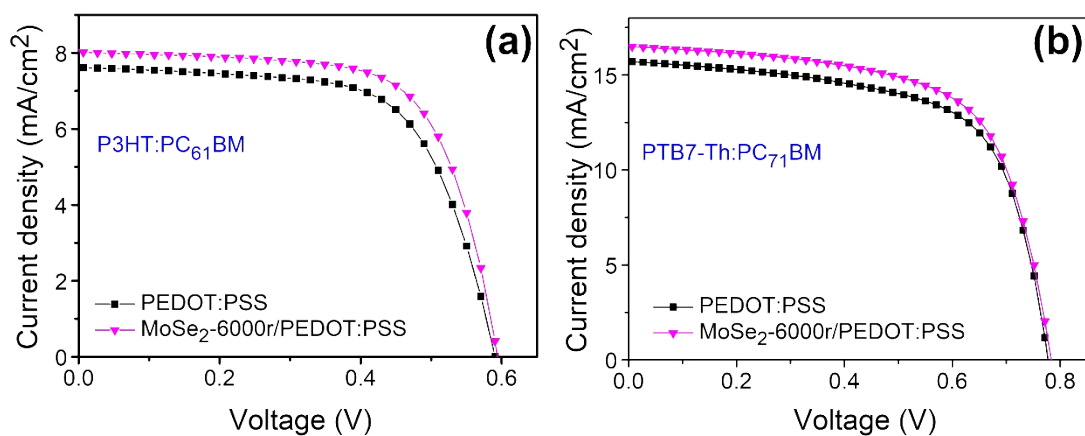
Fig. S13. *J–V* curves based on the blend system (a) P3HT/PC$_{61}$BM, and (b) PTB7-Th/PC$_{71}$BM.

Table S1. Parameters of the testing liquids of water and EG.

Liquid	Dispersion force [V_L^d]	Polar force [V_L^P]	Surface energy [V_L]
Water	22.1	50.7	72.8
EG	29.3	18.9	48.2

Table S2. The contact angle and surface energy of different materials.

Material	Water contact angle	EG contact angle	Surface energy [mN m - 1]
ITO	32.0°	23.0°	68.8
$MoSe_2$	30.0°	13.0°	70.0
PEDOT:PSS	17.0°	24.0°	85.5
$MoSe_2$/PEDOT:PSS	15.0°	22.0°	89.0
PM6:Y6	98.5°	64.0°	40.9

Table S3. The interface energy between two different materials.

Material	Interfacial energy [mN m - 1]
ITO/PEDOT:PSS	4.42
$MoSe_2$/PEDOT:PSS	7.54
PEDOT:PSS/PM6:Y6	121.0
$MoSe_2$/PEDOT:PSS/PM6:Y6	128.4

Table S4. Summary of device performances of PM6:Y6 based OSCs without or with $MoSe_2$ QDs with different rotation speeds.

Layer[a]	J_{sc} [mA cm^{-2}]	V_{oc} [V]	FF [%]	PCE [%]	R_s [Ω·cm^2]
PEDOT:PSS	24.68	0.84	74.29	15.48 (15.18±0.2)[b]	7.94
$MoSe_2$-4000r/PEDOT:PSS	25.68	0.83	73.76	15.68 (15.26±0.2)[b]	4.78
$MoSe_2$-5000r/PEDOT:PSS	25.83	0.83	74.34	15.92 (15.56±0.3)[b]	4.25
$MoSe_2$-6000r/PEDOT:PSS	25.84	0.83	74.69	16.08 (15.75±0.2)[b]	3.63
$MoSe_2$-7000r/PEDOT:PSS	25.69	0.83	75.03	16.00 (15.68±0.3)[b]	4.59

[a] For PEDOT:PSS, 3000 rotations per minute (r) were used. [b] Average PCE with standard deviations were obtained from 10 devices.

Table S5. Comparison of the device parameters of previously reported devices with 2D materials as the interface modifier.

Material	Synthetic method	Function of TMDs	Deposition method	Device structures	PCE (%)	Reference
WS$_2$	Sonication	HTL	Spin-coating	ITO/WS$_2$/P3HT:PCBM/LiF/Al	2.40	[1]
Bi$_2$Se$_3$	Lithium intercalation	HTL	Spin-coating	ITO/ZnO/P3HT:PC$_{61}$BM/L-Bi$_2$Se$_3$/Ag	4.37	[2]
MoS$_2$	Lithium intercalation	HTL	Spin-coating	ITO/MoS$_x$/P3HT:PCBM/LiF/Al	2.95	[3]
MoS$_2$	Lithium intercalation	HTL	Spin-coating	ITO/ZnO/P3HT:PCBM/MoS$_2$/Ag ITO/ZnO/PTB7:PC$_{71}$BM/MoS$_2$/Ag	4.02 8.11	[4]
NbSe$_2$	Lithium intercalation	HTL	Spin-coating	ITO/ZnO/PTB7:PC$_{71}$BM/NbSe$_2$/Ag	8.10	[5]
MoS$_2$	Sonication	HTL	Spin-coating	ITO/MoS$_2$/P3HT:PCBM/LiF/Al	2.44	[6]
MoS$_2$ WS$_2$	Sonication	HTL	Transferring	ITO/MoS$_x$/P3HT:PCBM/LiF/Al ITO/WS$_2$/P3HT:PCBM/LiF/Al	2.96 3.08	[7]
MoS$_2$	Lithium intercalation	HTL ETL	Spin-coating	ITO/p-doped MoS$_2$/P3HT:PCBM/Ca/Al ITO/n-doped MoS$_2$/P3HT:PCBM/PEDOT:PSS/Ag	3.38 2.73	[8]
In$_2$Se$_3$	Sonication	HTL	Spin-coating	ITO/α-In$_2$Se$_3$/PBDB-T:ITIC/Ca/Al	9.60	[9]
MoS$_2$	Sonication	ETL	Spin-coating	ITO/MoS$_2$/PTB7-Th:PC$_{71}$BM/MoO$_3$/Al	9.07	[10]
BP	Liquid-phase exfoliation	HTL/ETL	Spin-coating	ITO/ZnO/BPQD1/PTB7-Th:FOIC//BPQD2/MoO$_3$/Al	13.10	[11]
MoS$_2$	Lithium intercalation	HTL	Spin-coating	ITO/MoS$_2$/PTB7:PC$_{71}$BM/PFN/Al	7.26	[12]
MoS$_2$	Lithium intercalation	HTL	Spin-coating	ITO/MoS$_2$/PTB7:PC$_{71}$BM/PFN/Al	7.64	[13]
TaS$_2$	Sonication	HTL ETL	Spin-coating	ITO/TaS$_2$/P3HT:PCBM/LiF/Al ITO/TaS$_2$/P3HT:PCBM/MoO$_3$/Al	3.06 2.73	[14]
MoS$_2$	Lithium intercalation	ETL	Spray-coating	ITO/ZnO/P3HT:PCBM/MoS$_2$/Al	2.04	[15]
WSe$_2$	Liquid-phase exfoliation	Third component	Spin-coating	ITO/PFN/PTB7:WSe$_2$:PCBM/MoO$_3$/Al	9.28	[16]
MoS$_2$	Salt-assisted exfoliation	HTL	Spin-coating	ITO/MoS$_2$/PBDTTT-CF:PC$_{71}$BM/Ca/Al	6.90	[17]
MoSe$_2$	Liquid-phase exfoliation	Third component	Spin-coating	ITO/ZnO/PTB7-TH:PC$_{71}$BM:MoSe$_2$/MoO$_3$/Ag	10.44	[18]
MoS$_2$ WS$_2$	Liquid-phase exfoliation	HTL	Spin-coating	ITO/MoS$_2$/PBDB-T-SF:IT-4F/PFN-Br/Al ITO/WS$_2$/PM6:Y6/PFN-Br/Al	12.00 15.80	[19]
BiOCl	Sonication	HTL	Spin-coating	ITO/BiOCl/PTB7-Th:PC$_{71}$BM/PDINO/Al ITO/BiOCl/PM6:Y6/PDINO/Al	9.92 16.11	[20]
Bi$_2$O$_2$Se	Liquid-phase exfoliation	HTL	Spin-coating	ITO/ZnO/PBDB-T:ITIC:Bi$_2$O$_2$Se/MoO$_3$/Al ITO/ZnO/PM6:Y6:Bi$_2$O$_2$Se/MoO$_3$/Al	12.22 16.28	[21]
GO/G	Micromechanical exfoliation	HTL/ETL	Spin-coating	ITO/PEDOT:PSS-GO/PTQ10:IDIC-2F/PDINO-G/Al ITO/PEDOT:PSS-GO/PM6:Y6/PDINO-G/Al	13.01 16.52	[22]
In$_2$Se$_3$	Sonication	HTL	Spin-coating	ITO/PEDOT:PSS:In$_2$Se$_3$/PBDB-T:ITIC/PFN-Br/Al ITO/PEDOT:PSS:In$_2$Se$_3$/PM6:Y6/PFN-Br/Al	11.22 15.89	[23]
g-C3N4	Centrifugation	HTL	Spin-coating	ITO/g-C3N4:PEDOT:PSS/PM6:Y6/PFN-Br/Ag	16.38	[24]
MoSe$_2$	**Lithium intercalation**	**HTL**	**Spin-coating**	**ITO/MoSe$_2$/PEDOT:PSS/PM6:Y6/PFN-Br/Al** **ITO/MoSe$_2$/PEDOT:PSS/SZ2:N3/PFN-Br/Al**	**16.08** **17.08**	**This work**

Table S6. Hole mobility and conductivity of the hole-only devices as measured by SCLC

method and van der Pauw four-probe conductivity technique, respectively.

Device	Hole mobility μ_h [cm^2 V^{-1}s^{-1}]	Conductivity [S cm^{-1}]
ITO/PEDOT:PSS/PM6:Y6/MoO$_3$/Al	6.30×10^{-5}	6.23×10^{-4}
ITO/ MoSe$_2$ QDs/PEDOT:PSS/PM6:Y6/MoO$_3$/Al	2.26×10^{-4}	9.76×10^{-4}

Table S7. Photovoltaic parameters of the optimal OSCs based on PBDB-T/ITIC, PTB7-Th/PC$_{71}$BM, and P3HT/PC$_{61}$BM with and without MoSe$_2$ QDs.

BHJ	Description	J_{sc} [mA cm^{-2}]	V_{oc} [V]	FF [%]	PCE [%]
PBDB-T:ITIC	PEDOT:PSS	15.40 (15.32±0.2)	0.89 (0.88±0.01)	69.55 (69.55±2.01)	9.51 (9.21±0.05)
	MoSe$_2$/PEDOT:PSS	16.18 (15.48±0.2)	0.90 (0.89±0.02)	72.30 (72.19±1.08)	10.41 (9.86±0.09)
PTB7-Th:PC$_{71}$BM	PEDOT:PSS	15.71 (15.66±0.3)	0.78 (0.77±0.01)	64.45 (62.07±3.12)	7.88 (7.49±0.07)
	MoSe$_2$/PEDOT:PSS	16.51 (16.34±0.2)	0.78 (0.78±0.01)	64.30 (62.12±2.06)	8.32 (7.92±0.08)
P3HT:PC$_{61}$BM	PEDOT:PSS	7.51 (7.26±0.3)	0.58 (0.58±0.01)	65.04 (63.86±1.06)	2.93 (2.77±0.14)
	MoSe$_2$/PEDOT:PSS	8.02 (7.58±0.2)	0.59 (0.58±0.01)	63.58 (62.16±1.02)	3.24 (2.98±0.16)

S1. Experimental details

1.1 Materials

PEDOT:PSS (Clevios PVP AI 4083, a weight ratio of 1:6) and MoSe$_2$ bulk material were bought from H.C. Starck. (2,2′-((2Z,2'Z)-((12,13-bis(3-ethylheptyl)-3,9-diundecyl-12,13-dihydro[1,2,5]thiadiazolo[3,4-e]thieno[2″,3‴:4',5']thieno[2′,3':4,5]pyrrolo[3,2-g]thieno[2′,3':4,5]thieno[3,2-b]indole-2,10-diyl)bis(methanylylidene))bis(5,6-difluoro-3-oxo-2,3-

dihydro-1H-indene-2,1-diylidene))dimalononitrile (N3), SZ2 (as donor material), (poly[(2,6-(4,8-bis(5-(2-ethylhexyl-3-fluoro)thiophen-2-yl)-benzo[1,2-b:4,5-b']dithiophene))-alt-(5,5-(1',3'-di2-thienyl-5',7'-bis(2-ethylhexyl)benzo[1',2'-c:4',5'-c']dithiophene-4,8-dione)]), (PM6) and (2,20-((2Z,20Z)-((12,13-bis(2-ethylhexyl)-3,9-diundecyl-12,13-dihydro-[1,2,5]thiadiazolo[3,4-e]thieno[200,300:40,50]thieno[20,30:4,5]pyrrolo[3,2-g]thieno[20,30:4,5]thieno[3,2-b]indole-2,10-diyl)bis (methanylylidene))-bis(5,6-diiluoro-3-oxo-2,3-dihydro-1H-indene-2,1- diylidene))dimalononitrile) (Y6) were purchased from eFlexPV Limited Inc. Poly[(2,6-(4,8-bis(5-(2-ethylhexyl)thiophen-2-yl)benzo[1,2-b:4,5-b']dithiophene)-co-(1,3-di(5-thiophene-2-yl)-5,7-bis(2-ethylhexyl)benzo[1,2-c:4,5-c']dithiophene-4,8-dione)] (PBDB-T), 3,9-bis(2-methylene(3-(1,1-dicyanomethylene) -indanone))-5,5,11,11-tetrakis(4-hexylphenyl)dithieno-[2,3-d:2′,3′-d′]-s-indaceno[1,2-b:5,6-b′]dithiophene (ITIC), poly[9,9-bis(6′-bromohexyl)fluorene-alt-co-1,4-phenylene (PFN-Br) were obtained from Solarmer Materials Inc. Poly({4,8-bis[(2-ethylhexyl)oxy]benzo[1,2-b:4,5-b′]dithiophene-2,6-diyl}{3-fluoro-2-[(2-ethylhexyl)-carbonyl]thieno[3,4-b]thiophenediyl}) (PTB7-Th), [6,6]-phenyl-C_{71}-butyricacid methyl ester (PC$_{71}$BM), poly(3-hexylthiophene) (P3HT) and [6,6]phenyl-C_{61}-butyric acid methyl ester (PC$_{61}$BM) were purchased from 1-Material Inc.1-chloronaphthalene (CN) and chlorobenzene (CB) were supplied by Sigma-Aldrich. All these commercial materials were used directly without further treatment.

1.2 Synthesis of MoSe$_2$ QDs

MoSe$_2$ QDs were synthesized using a lithium intercalation method as reported previously in the literature.[33] In the glove box, 0.5 g MoSe$_2$ bulk material was added into 5 mL of 2.2M n-butyl lithium solution and stirred evenly for two days, so that lithium ions

could fully enter into the interlayers of the MoSe$_2$ bulk material and form the Li$_x$MoSe$_2$ species. Then the Li$_x$MoSe$_2$ compound was retrieved by filtration and washed with hexane several times to remove excess lithium and organic residues. Li$_x$MoSe$_2$ was ultrasonicated in water for 3 h and the mixture was dialyzed in water for 2 days to remove LiOH and unexfoliated materials. The as-prepared MoSe$_2$ QDs that emitted weak blue fluorescence were collected by further centrifugation at 12,000 rpm for 20 min. The sample was diluted with deionized water to a concentration of about 0.5 mg/mL for device fabrication.

1.3 Device fabrication

OSCs were fabricated on a patterned ITO/glass substrate with a sheet resistance of 20 Ω/square. Substrates were cleaned via sonication sequentially in deionized water, acetone and isopropanol for 20 min, and then dried using a pure nitrogen gas stream and exposed to UV-ozone for 15 min prior to the device fabrication. The MoSe$_2$ QDs solution was first spin coated on the ITO substrate at different speeds (4000-7000 rpm) for 60 s and then annealed on a hot plate at 300 ℃ for 15 min in air to remove the water. Next, as-received PEDOT:PSS suspensions were subsequently spin-coated onto the above substrates at 4000 rpm for 60 s (thickness ∼ 40 nm), and then annealed at 130 ℃ for 20 min in air. Afterwards, the substrates were transferred into a N$_2$-filled glove box. The pre-prepared active layer (PM6:Y6 dissolved in CN) blend solution were spin coated (2000 rpm, 30 s) on the HEL films in the N$_2$-filled glove box, followed by heating at 100 ℃ for 10 min. After that, PFN-Br dissolved in methanol (0.5 mg mL^{-1}) and was spun on top of the BHJ layer at 4000 rpm for 30s. Finally, the samples were transferred into a thermal vacuum evaporator for the deposition of Al (100 nm) under high vacuum (5.0×10^{-4} Pa). The active area of the pixel was approximately 4 mm^2,

which was strictly patterned by a shadow mask. For the sake of comparison, structurally identical control OSCs with a pure PEDOT:PSS anode contact were also fabricated.

1.4 Device Characterization

The intensity of the solar simulator was determined by a standard Si photovoltaic cell calibrated by the National Renewable Energy Laboratory. The current density (J)-voltage (V) characteristics were recorded with a Keithley 2420 source meter in the dark and under illumination using a solar simulator with an AM 1.5G simulated solar spectrum. The J–V curve of the device is measured every 30 s. The measurement interval is 20 mV. The EQE spectra were measured using a 7-SCSpec solar cell measurement system. All the measurements were performed in air under ambient conditions without device encapsulation. The dependence curve of the J–V under different light intensities was measured using a standard Si solar cell combination with a neutral density sieve.

The atomic force microscopic (AFM) images and scanning electron microscopic (SEM) images were collected using a Nanonavi SPA-400SPM AFM in the tapping mode and a Philips scanning electron microscope, respectively. Transmission electron microscopy (TEM) and high-resolution TEM (HR-TEM) images were recorded by JEM-2100F and energy dispersive X-ray spectroscopy (EDS) operated at 200 kV. The UV-visible absorption and transmission spectra were taken with UV–vis spectrophotometer (HP 8453). A Hitachi F-7000 spectrofluorophotometer was utilized for the photoluminescence (PL) spectra. The TRPL spectra were measured by the FLS980 Spectrometer. The X-ray photoelectron spectra (XPS) and ultraviolet photoelectron spectra (UPS) were obtained with an Axis Ultra DLD X-ray photoelectron spectrometer equipped with an Al Kα X-ray source (1486.6 eV) and He I

(21.22 eV), respectively. The grazing incidence small-angle X-ray scattering (GISAXS) and grazing incidence wide-angle X-ray scattering (GIWAXS) measurements of the pre-prepared samples were performed using an incident angle of 0.2° at the BL14B station of the Shanghai Synchrotron Radiation Facility (SSRF). The electrochemical impedance spectroscopy (EIS) was measured using an electrochemical workstation in the frequency range between 0.1 Hz and 1.0 MHz

S2. The XPS characterization of post heat-treated thin film of $MoSe_2$ QDs

By analyzing the peak areas of 3d peaks of Mo and Se, the Mo:Se ratio was calculated to be 1:1.76, which is less than the nominal value of 1:2, indicating the presence of a large amount of selenium vacancies and edge structures in $MoSe_2$ QDs. The peaks at 228.3 and 231.4 eV are inferred from Mo^{4+} $3d_{5/2}$ and Mo^{4+} $3d_{3/2}$, respectively, while the peaks at 54.6 and 55.4 eV can be attributed to Se^{2-} $3d_{5/2}$ and Se^{2-} $3d_{3/2}$ orbits, which match well with the 2H-$MoSe_2$ QDs phase.[25] As a result, we induced that there are a few MoO_3 species existing, probably at the $MoSe_2$/PEDOT:PSS interface. Compared to the previous reports, the significant oxidation in $MoSe_2$ QDs as confirmed by peaks of Mo^{6+} and Se^{4+} in XPS spectra is attributed to the high-temperature annealing process of $MoSe_2$ QDs.[26] Fig. S2c shows O 1s core level peaks in 530.7 and 528.9 eV, fitted with the Gaussian–Lorentzian function, corresponding to the adsorbed oxygen and lattice oxygen, respectively. The former is mainly physically adsorbed due to the electronegativity of $MoSe_2$ QDs, which can easily disappear in a high vacuum condition. The latter is derived from the redox reaction of the $MoSe_2$ QDs. It is reported that the O incorporation not only could partially fill the Se vacancies and passivate the structural defects, but lead to a change of interfacial energy level alignment (change n-

type MoSe$_2$ to p-type), which is beneficial to device efficiency and stability (see Fig. 2d).[27]

Based on the above discussion, we suspect that Mo^{6+} mainly comes from the oxidation of the selenium vacancies and edge structures and speculate that the reaction equation is as follows:

$$MoSe_2 + O_2 \rightarrow MoO_3 + MoSe_xO_{3-x} + SeO_2 \ (0<x<3)$$

S3. The calculation of G_{max} and P(E,T)

J_{ph} is defined as $J_{light} - J_{dark}$, where J_{light} and J_{dark} are the current densities under illumination and in dark state, respectively.[29] V_{eff} is determined as $V_{eff} = V_0 - V_{app}$, where V_0 is the built-in potential and V_{app} is the applied bias voltage. The curve is divided into two distinct regions. J_{ph} firstly increases almost linearly with V_{eff} in the low effective voltage regime. Then, it gradually reaches a saturated photocurrent (J_{sat}) when $V_{eff} \geq 0.2$ V. Assuming that all the photogenerated excitons are dissociated into free charge carriers and collected without the recombination loss under the high effective voltage, then the maximum exciton generation rate (G_{max}) could be determined by the equation $J_{sat} = qG_{max}L$, where q is the elementary charge and L is the BHJ thickness.[28] The values of G_{max} based on PEDOT:PSS and MoSe$_2$ QDs/PEDOT:PSS HEL are calculated to be 9.65×10^{27} m^{-3} s^{-1} for control cell, 1.04×10^{28} m^{-3} s^{-1} for MoSe$_2$ QDs-4000r/PEDOT:PSS, 1.05×10^{28} m^{-3} s^{-1} for MoSe$_2$ QDs-5000r/PEDOT:PSS, 1.07×10^{28} m^{-3} s^{-1} for MoSe$_2$ QDs-6000r/PEDOT:PSS, and 1.06×10^{28} m^{-3} s^{-1} for MoSe$_2$ QDs-7000r/PEDOT:PSS, respectively, as shown in Fig. S5b. The enhanced G_{max} indicates that the embedded MoSe$_2$ QDs can promote light absorption in OSCs, leading to the increase of J_{sc} values. The exciton dissociation probabilities $P(E,T)$ are estimated according to the following relationship: $J_{ph} = qG_{max} P(E,T)L$. The $P(E,T)$ can also be obtained from the ratio of J_{ph}/J_{sat}. It turns out that the value of $P(E,T)$ increases from 88.6% of the

control cell to 93.8% of the MoSe$_2$ QDs-6000r/PEDOT:PSS-based cell, indicating that introduction of MoSe$_2$ QDs into cells contributes to improving the overall charge dissociation process and reducing charge recombination, and thereby achieving high PCE.

S4. The relationship of J_{sc}, V_{oc} and I

The relationship between J_{sc} and I can be described as $J_{sc} \propto I^\alpha$, where α is the index factor. A weaker bimolecular recombination process can be anticipated for the OSC device if the value of α is approaching to 1.[29] The relationship between V_{oc} and I can be expressed by the equation of $V_{oc} \propto n\, kT/q\, ln(I)$, where k, T, and q are the Boltzmann constant, the temperature in K, and the elementary charge, respectively.[30] When bimolecular recombination dominates in the cell, the slope would be close to 1 kT/q, while for monomolecular recombination (trap-assisted recombination) dominated cell, the slope would be close to 2 kT/q.[11]

S5. The surface energy and interfacial energy calculations

The surface energy is calculated by using the following equation:

$$V_L = V_L^d + V_L^p \qquad\qquad \text{S5-1}$$

$$1 + cos\theta = 2(\sqrt{V_L^d} \cdot \frac{\sqrt{V_L^d}}{V_L} + \sqrt{V_L^p} \cdot \frac{\sqrt{V_L^p}}{V_L}) \qquad\qquad \text{S5-2}$$

where V_L represents pure material surface energy, V^d and V^P are dispersion force and polarity force. Surface energy (V_L) was determined by the contact angles of the testing liquids of water and EG, and the parameters of the testing liquids as Table S1-S3 as shown above. In light of the surface energy of two different materials, interfacial energy between two different materials can be determined according to the equation below:

$$V_{A-B} = V_A + V_B - 4\left(\frac{V_A^d \cdot V_B^d}{V_A^d + V_B^d} + \frac{V_A^p \cdot V_B^p}{V_A^p + V_B^p}\right)$$
$$\text{S5-3}$$

where V_A and V_B represent the surface energy of sample A and sample B, respectively; V_A^d and V_B^d are dispersion forces of sample A and sample B, respectively; V_A^p and V_B^p are polarity forces of sample A and sample B, respectively.

References

1.   Q. V. Le, T. P. Nguyen and S. Y. Kim, Phys. *Status Solidi RRL.*, 2014, **8**, 390-394.

2.   Z. Yuan, Z. Wu, S. Bai, W. Cui, J. Liu, T. Song and B. Sun, *Org. Electron.*, 2015, **26**, 327-333.

3.   Q. Van Le, T. P. Nguyen, M. Park, W. Sohn, H. W. Jang and S. Y. Kim, *Adv. Opt. Mater.*, 2016, **4**, 1796-1804.

4.   X. Gu, W. Cui, H. Li, Z. Wu, Z. Zeng, S.-T. Lee, H. Zhang and B. Sun, *Adv. Energy Mater.*, 2013, **3**, 1262-1268.

5.   X. Gu, W. Cui, T. Song, C. Liu, X. Shi, S. Wang and B. Sun, *ChemSusChem*, 2014, **7**, 416-420.

6.   Q. V. Le, T. P. Nguyen, H. W. Jang and S. Y. Kim, *Phys. Chem. Chem. Phys.*, 2014, **16**, 13123-13128.

7.   K. C. Kwon, C. Kim, Q. V. Le, S. Gim, J.-M. Jeon, J. Y. Ham, J.-L. Lee, H. W. Jang and S. Y. Kim, *ACS Nano*, 2015, **9**, 4146-4155.

8.   J.-M. Yun, Y.-J. Noh, J.-S. Yeo, Y.-J. Go, S.-I. Na, H.-G. Jeong, J. Kim, S. Lee, S.-S. Kim, H. Y. Koo, T.-W. Kim and D.-Y. Kim, *J. Mater. Chem. C*, 2013, **1**, 3777-3783.

9.   J. Wang, H. Yu, C. Hou and J. Zhang, *Solar RRL*, 2020, **4**, 1900428.

10. K. S. Lee, Y. J. Park, J. Shim, C.-H. Lee, G.-H. Lim, H. Y. Kim, J. W. Choi, C.-L. Lee, Y. Jin, K. Yu, H.-S. Chung, B. Angadi, S.-I. Na and D. I. Son, *J. Mater. Chem. A*, 2019, **7**, 15356-15363.

11. Y. Wang, J. Li, T. Li, J. Wang, K. Liu, Q. Jiang, J. Tang and X. Zhan, Small, 2019, 15, 1903977.

12. W. Liu, X. Yang, Y. Zhang, M. Xu and H. Chen, *RSC Adv.*, 2014, **3**, 32744.

13. X. Yang, W. Fu, W. Liu, J. Hong, Y. Cai, C. Jin, M. Xu, H. Wang, D. Yang and H. Chen, *J. Mater. Chem. A*, 2014, **2**, 7727-7733.

14. Q. V. Le, T. P. Nguyen, K. S. Choi, Y.-H. Cho, Y. J. Hong and S. Y. Kim, *Phys. Chem. Chem. Phys.*, 2014, **16**, 25468-25472.

15. D. Barrera, A. Jawaid, T. B. Daunis, L. Cheng, Q. Wang, Y.-J. Lee, M. J. Kim, J. Kim, R. A. Vaia and J. W. P. Hsu, *Mater. Today Energy*, 2017, **5**, 107-111.

16. G. Kakavelakis, A. E. Del Rio Castillo, V. Pellegrini, A. Ansaldo, P. Tzourmpakis, R. Brescia, M. Prato, E. Stratakis, E. Kymakis and F. Bonaccorso, *ACS Nano*, 2017, **11**, 3517-3531.

17. H.-C. Wang, Y.-C. Lin, C.-H. Chen, C.-H. Huang, B. Chang, Y.-L. Liu, H.-W. Cheng, C.-S. Tsao and K.-H. Wei, *Nanoscale*, 2019, **11**, 17460-17470.

18. J.-M. Yun, Y.-J. Noh, C.-H. Lee, S.-I. Na, S. Lee, S. M. Jo, H.-I. Joh and D.-Y. Kim, *Small*, 2014, **10**, 2319-2324.

19. Y. Lin, B. Adilbekova, Y. Firdaus, E. Yengel, H. Faber, M. Sajjad, X. Zheng, E. Yarali, A. Seitkhan, O. M. Bakr, A. El-Labban, U. Schwingenschlögl, V. Tung, I. McCulloch, F. Laquai and T. D. Anthopoulos, *Adv. Mater.*, 2019, **31**, 1902965.

20. B. Liu, Y. Wang, P. Chen, X. Zhang, H. Sun, Y. Tang, Q. Liao, J. Huang, H. Wang, H. Meng and X. Guo, *ACS Appl. Mater. Interfaces*, 2019, **11**, 33505-33514.

21. C. Huang and H. Yu, *ACS Appl. Mater. Interfaces*, 2020, **12**, 19643-19654.

22. F. Pan, C. Sun, Y. Li, D. Tang, Y. Zou, X. Li, S. Bai, X. Wei, M. Lv, X. Chen and Y. Li, *Energy Environ. Sci.*, 2019, **12**, 3400-3411.

23. J. Wang, H. Yu, C. Hou and J. Zhang, *ACS Appl. Mater. Interfaces*, 2020, **12**, 26543-26554.

24. Q. Yang, S. Yu, P. Fu, W. Yu, Y. Liu, X. Liu, Z. Feng, X. Guo and C. Li, *Adv. Funct. Mater.*, 2020, **30**, 1910205.

25. L. Yuwen, J. Zhou, Y. Zhang, Q. Zhang, J. Shan, Z. Luo, L. Weng, Z. Teng and L. Wang, *Nanoscale*, 2016, **8**, 2720-2726.

26. C. Xu, S. Peng, C. Tan, H. Ang, H. Tan, H. Zhang and Q. Yan, *J. Mater. Chem. A*, 2014, **2**, 5597-5601.

27. L. Liu, Y. Kan, K. Gao, J. Wang, M. Zhao, H. Chen, C. Zhao, T. Jiu, A.-K.-Y. Jen and Y. Li, *Adv. Mater.*, 2020, **32**, 1907604.

28. J. Xiao, M. Ren, G. Zhang, J. Wang, D. Zhang, L. Liu, N. Li, C. J. Brabec, H.-L. Yip and Y. Cao, *Solar RRL*, 2019, **3**, 1900077.

29. L. J. A. Koster, V. D. Mihailetchi, R. Ramaker and P. W. M. Blom, *Appl. Phys. Lett.*, 2005, **86**, 123509.

30. S. R. Cowan, A. Roy and A. J. Heeger, *Phys. Rev. B*, 2010, **82**, 245207.